

Ultralong Imaging Range Chromatic Confocal Microscopy

Gargi Sharma* and Kanwarpal Singh

Confocal microscopy is regularly used in cellular research but unfortunately, the imaging is restricted to a single plane. Chromatic confocal microscopy (CCM) offers the possibility to image multiple planes simultaneously, thus providing a manifold increase in the imaging speed, whereas eliminating the need for z-axis scanning. Standard chromatic confocal systems have a limited imaging range of the order of a few hundreds of micrometers which limits their applications. Herein, using a single zinc selenide lens, a CCM system that has an imaging range of 18 mm (± 68 nm) with an average spatial resolution of 2.46 μm (± 44 nm) and another system with a 1.55 mm (± 14 nm) imaging range with 0.86 μm (± 30 nm) average lateral spatial resolution is demonstrated. In doing so, sevenfold increase in the imaging range for the system with 1.55 mm imaging when compared with previously reported systems with similar lateral spatial resolution is achieved. The proposed approach can be a powerful tool for confocal imaging of biological samples or surface profiling of industrial samples.

1. Introduction

Visualization of the cellular and subcellular structures within the tissue has helped the biomedical community to understand and identify the very nature of these entities. Many times, the anomaly initiates not at the surface but beneath. For such cases, cellular level, 3D imaging is required for early disease diagnosis. Recent 3D microscopy techniques allow one to visualize cellular features beneath the surface. High-resolution 3D imaging techniques like optical coherence tomography (OCT),^[1] confocal microscopy,^[2] chromatic confocal microscopy (CCM),^[3] light sheet microscopy,^[4] etc. have been developed in this direction.

OCT provides 3D information of the sample based on low-coherence interferometry of light. Using OCT, one may achieve an axial and lateral spatial resolution of a few micrometers. Even though OCT can achieve cellular-level lateral spatial

resolution,^[5] it is maintained in the focal plane only, and as one moves above or below the focus, the resolution drops significantly. Light sheet microscopy^[4] can provide high-contrast sample images from a focal plane but owing to its complex architecture has limited in vivo applications. Confocal microscopy has been the technique of choice for biologists for cellular tomography with lateral spatial resolution below 1 μm .^[6] Standard confocal microscopy is a point scanning method, and one would need to scan X-, Y-, and Z-axis to acquire the complete tomographic information, which increases the scanning time significantly.^[7] To reduce the scanning time, multiplane confocal microscopy techniques^[8,9] suitable for imaging two^[8] or four planes^[9] simultaneously have been developed. Fast scanning along Z-axis has


also been achieved using tunable lenses.^[10,11] Spinning disc confocal microscopy^[12] has increased the scanning speeds to a level that up to 1000 frames can be acquired in less than a second; such systems however are still very bulky and only used as bench-top imaging systems. To overcome this limitation, techniques like CCM^[3,13–25] have been developed. Using the chromatic dispersion property of light, one may extend the imaging range with a comparable lateral spatial resolution to that of confocal microscopy. Recently, specially fabricated metalenses^[18] have been used for CCM, achieving an imaging range of 33.5 μm but manufacturing of such lenses is still limited to specialized facilities. To the best of our knowledge, a maximum imaging range of 250 μm has been achieved using chromatic aberration of multiple achromatic and diffractive lenses where an average lateral spatial resolution of around 1 μm is maintained within the imaging range.^[25]

An ideal 3D microscopy imaging system should be able to provide a lateral spatial resolution that allows cellular-level imaging at the maximum possible imaging range. Generally speaking, one may improve the resolution in the aforementioned techniques using a high-numerical-aperture (NA) lens but this comes at the expense of reduced imaging range. A higher imaging range can be achieved using a lower-NA objective but then the lateral spatial resolution is compromised. Therefore, current advancements in this direction suffer from a trade-off between the imaging range and the resolution. Unfortunately, we still lack a 3D microscopy technique that has a superior lateral spatial and axial spatial resolution and a large imaging range to visualize cellular structures in biological samples.

In this work, we utilized the exceptionally high chromatic dispersion property of the zinc selenide (ZnSe) material-based lens to focus different wavelength components of a supercontinuum

G. Sharma, K. Singh
Max Planck Institute for the Science of Light
Staudtstraße 2, 91058 Erlangen, Germany
E-mail: Gargi.Sharma@mpl.mpg.de

K. Singh
Department of Physics
Friedrich Alexander University Erlangen-Nürnberg
Erlangen, Germany

 The ORCID identification number(s) for the author(s) of this article can be found under <https://doi.org/10.1002/adpr.202200116>.

© 2022 The Authors. Advanced Photonics Research published by Wiley-VCH GmbH. This is an open access article under the terms of the Creative Commons Attribution License, which permits use, distribution and reproduction in any medium, provided the original work is properly cited.

DOI: 10.1002/adpr.202200116

light source (SCL) at different axial positions to develop a CCM system. We demonstrate the suitability of this system to image biological samples with cellular resolution by imaging a swine cornea ex vivo. As CCM systems can also be used to perform surface profiling of industrial samples, we show the surface profile of a microfluidic channel acquired with our system.

2. Results

2.1. System Characterization

The optical response of an aspheric ZnSe lens was first simulated using OpticStudio (Zemax, UK). The simulation results for 6.35 mm (39469, Edmund Optics, UK), 12.7 mm (39471, Edmund Optics, UK), and 50.8 mm (39495, Edmund Optics,

Table 1. Simulations for the comparison of different focal length ZnSe lenses for the imaging range, the lateral spatial resolution, and the EDRR.

Lens	Wavelength	Focal position [mm]	Lateral spatial resolution [μm]	EDRR
39469 (6.35 mm focal length)	500 nm	5.5	0.7	–
	700 nm	6.57	1.08	–
	950 nm	7.07	1.57	–
		Imaging range (1.57 mm)	Avg (1.11)	1414
39471 (12.7 mm focal length)	500 nm	12.4	0.8	–
	700 nm	14.9	1.4	–
	950 nm	15.8	2.1	–
		Imaging range (3.4 mm)	Avg (1.43)	2377
39495 (50.8 mm focal length)	500 nm	64.4	1.5	–
	700 nm	78.2	2.75	–
	950 nm	83.78	3.2	–
		Imaging range (19.38 mm)	Avg (2.48)	7814

Table 2. Previously reported chromatic confocal microscopy systems with the corresponding average lateral spatial resolution, average axial spatial resolution, imaging range, and EDRR.

Group	Resolution lateral [μm]	Resolution axial [μm]	Imaging range [μm]	EDRR spatial	EDRR axial
Current system	0.87	8.6	1550	1781.6	180.2
Garzón et al. 2008 ^[25]	0.98	Not provided	250	255.1	Not applicable
Olsovsky et al. 2013 ^[16]	0.70	3.1	157	224.3	50.65
Garzón et al. 2004 ^[24]	1.10	6.9	200	181.8	28.9
Kim et al. 2013 ^[23]	0.98	Not provided	108	110.2	Not applicable
Chun et al. 2009 ^[22]	0.73	12.8	69	94.5	5.39
Li et al. 2020 ^[17]	0.81	12.63	45	55.5	3.5
Chen et al. 2019 ^[18]	0.77	6.7	33.5	43.2	5
Cha et al. 2000 ^[15]	Not provided	1.03	26.4	Not applicable	25.6
Lyda et al. 2012 ^[21]	2.00	Not provided	35	17.5	Not applicable
Tiziani et al. 1994 ^[13]	0.42	Not provided	5.1	12.1	Not applicable
Shi et al. 2004 ^[3]	1.00	0.675	7.0	7.0	10.3

UK) focal length lenses at 500 nm, 700 nm, and 950 nm wavelengths are shown in **Table 1**. Different wavelength components focus at different positions because of the high chromatic dispersion of the ZnSe lens. From the simulated focal position for 500, 700, and 950 nm wavelengths, we calculated the imaging range, which is the distance between the focal positions of the 500 nm and the 950 nm wavelength. From the focused spot, we calculated the lateral spatial resolution which is defined as the full width half maxima (FWHM) of the focal spot in the lateral direction. For all three lenses, we also calculated a parameter called extended depth resolution ratio (EDRR), which is the ratio of the imaging range and the average resolution in that region.

From the simulations, it is evident that the lateral spatial resolution, ranging between 0.7 and 1.57 μm for 500–950 nm wavelengths, can be achieved by using a 6.35 mm focal length lens with an imaging range of 1.57 mm. The EDRR for the 6.35 mm focal length lens comes out to be 1414. The imaging range can be increased to 3.4 mm using a 12.7 mm focal length lens, and can be increased further up to 19.38 mm using a 50.8 mm focal length lens, with an EDRR of 2377 and 7814, respectively. The reader should note that the calculated EDRR values are for the air and would depend on the refractive index of the medium. We have also compared the average lateral spatial resolution, average axial spatial resolution, the imaging range, and the EDRR of previously reported chromatic confocal systems in **Table 2** where axial spatial resolution is defined as the FWHM of the focused spot in the axial direction.

To experimentally demonstrate the capability of the ZnSe-based CCM system, we chose 6.35 and 50.8 mm focal length lenses as one provides better resolution and the other provides a larger imaging range. The object space NA for 6.35 and 50.8 mm focal length lenses at 700 nm wavelength was measured to be 0.52 and 0.16, respectively, with an effective focal length of 6.5 and 77.9 mm, respectively. We characterized the 50.8 mm focal length, ZnSe lens-based CCM system by measuring the imaging range, the lateral spatial resolution, and the axial spatial resolution.

We used a mirror as a sample and placed it on a translational stage. The mirror was axially translated using the stage and the

reflected wavelength as a function of stage position was recorded. The axial focal position of different wavelength components over the wavelength range is shown in **Figure 1a**. We achieved an imaging range of 18 mm for the wavelength components from 500 and 950 nm which is in close agreement with the simulations. In **Figure 1b**, we show the experimental lateral spatial resolution across the entire imaging range. The lateral spatial resolution was measured using the knife-edge technique.^[26] The knife-edge measurement was performed by traversing the resolution target (R1L3S6P, Thorlabs Inc., USA) with 50 nm steps using an automated translation stage. The distance traveled by the stage between the 90% beam power transmission and 10% beam power transmission was measured and multiplied by 1.561 to acquire the focused beam diameter.^[26] **Figure 1c** shows the measured axial spatial resolution as a function of the axial position. For the 50.8 mm focal length, ZnSe lens-based CCM system, we could achieve an average lateral spatial resolution of $2.46 \mu\text{m}$ ($\pm 44 \text{ nm}$) and average axial spatial resolution of $99.4 \mu\text{m}$ ($\pm 68 \text{ nm}$) where the averaging is performed on measurement points separated equally in distance space. The axial spatial resolution was measured as FWHM of the axial point spread function which was obtained by placing a mirror as a sample at different depths.

Since for the biological samples, better resolution is more desirable, we designed a CCM system using a 6.35 mm focal length ZnSe lens (39469, Edmund Optics, UK) which was used for imaging various samples. The system was designed and characterized theoretically and experimentally for different parameters like chromatic axial separation over the bandwidth of the light source, axial, and lateral spatial resolution. The axial separation between various wavelength components as a function of wavelength was calculated theoretically and measured experimentally and is plotted in **Figure 2**. As shown in **Figure 2a**, the wavelengths from 500 nm to 950 nm are axially separated over a distance of 1.55 mm ($\pm 14 \text{ nm}$). In **Figure 2b** we show the position of the reflected signal from a mirror at different distances as a function of camera pixel numbers after the reflected signal has passed through a prism, a lens, and focused on the camera.

The lateral spatial resolution for the 6.35 mm ZnSe lens-based CCM device was measured experimentally using the knife-edge technique.^[26] The experimentally measured lateral spatial resolution is plotted in **Figure 2c**. The best lateral spatial resolution was

measured to be $0.7 \mu\text{m}$ ($\pm 28 \text{ nm}$) at 500 nm wavelength and was maintained below $1 \mu\text{m}$ up to 735 nm, which corresponds to a depth of $\approx 1.2 \text{ mm}$. For 950 nm wavelength, the lateral spatial resolution increased to $1.77 \mu\text{m}$ ($\pm 36 \text{ nm}$). The average lateral spatial resolution with the 6.35 mm focal length ZnSe lens was found to be $0.87 \mu\text{m}$ ($\pm 30 \text{ nm}$), where the measurement points are equally separated in distance along the axial direction. Further, we imaged the USAF resolution target (R1S1L1N, Thorlabs Inc., USA) at 950 nm wavelength and could identify all the six elements of group seven, as shown in **Figure 2e**. This corresponds to a lateral spatial resolution better than $2 \mu\text{m}$ which was maintained for the whole imaging range.

We also measured the axial spatial resolution which determines the optical sectioning capability of the CCM device. The measured axial spatial resolution as a function of the axial position is shown in **Figure 2d**. Within the wavelength range of 500–950 nm, the axial spatial resolution varies from 5 to 25 μm . The average axial spatial resolution was found to be $8.6 \mu\text{m}$ ($\pm 30 \text{ nm}$) over the entire imaging range where data points are equally separated in distance along the axial direction.

To demonstrate the high-resolution depth imaging capability of the CCM device, we performed volumetric imaging of an iron oxide nanoparticles phantom with particle size $< 1 \mu\text{m}$. The focused beam on the phantom was scanned using an amplified piezoelectric actuator along the fast imaging axis and using a precision translation stage along the slow imaging axis to obtain the volumetric image data. The volumetric image of the phantom is shown in **Figure 3a**. The phantom was imaged for a $0.5 \text{ mm} \times 0.5 \text{ mm}$ area with a depth of around 1.5 mm (limited by the depth range of our device). The enface images of the iron oxide nanoparticles at depths of 0.35, 0.9, and 1.3 mm are shown in **Figure 3b–d**, respectively. The corresponding X and Y intensity profiles of the visibly smallest oxide nanoparticles are plotted in **Figure 3e–g**, respectively. The Z-axis profiles of the visibly smallest oxide nanoparticle at depths of 0.35, 0.9, and 1.3 mm are plotted in **Figure 3h–j**, respectively. At a depth of 0.35 mm, the lateral size of the oxide nanoparticle is measured to be better than $1 \mu\text{m}$ in X-axis and Y-axis. The lateral size of the smallest nanoparticle at a depth of 0.9 mm was also measured to be of the order of $1 \mu\text{m}$. The measured lateral size of the nanoparticle increased to $\approx 1.8 \mu\text{m}$ at a depth of 1.3 mm. The measured lateral spatial resolution of the nanoparticles was found to be $\approx 21\%$, 37% , and 80% larger than the lateral spatial resolution measured in

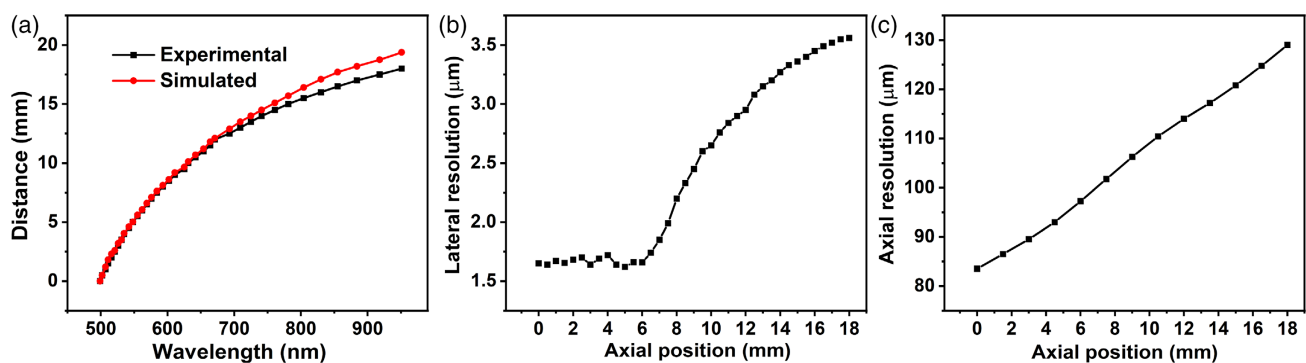


Figure 1. Characterization of 50.8 mm focal length, ZnSe lens-based CCM system. a) The graph plotted between the focal distance and wavelength. b) The experimental lateral spatial resolution as a function of wavelength. c) Experimental axial spatial resolution.

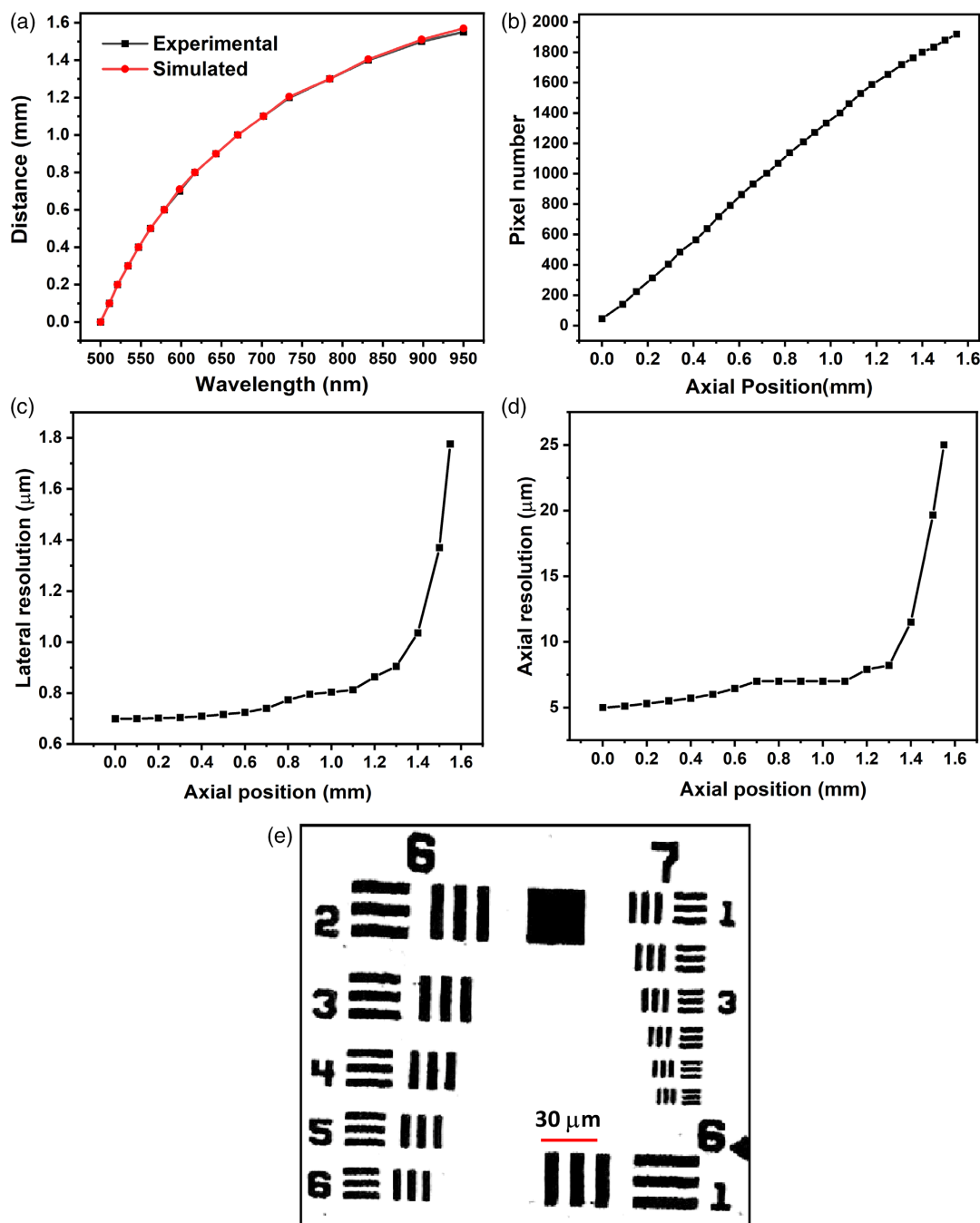


Figure 2. Characterization of 6.35 mm ZnSe lens-based CCM system. a) The graph plotted between the wavelength and their corresponding focal distance. b) The position of the reflected signal at the camera pixel number with respect to the axial position of the reflecting mirror. c) The experimental lateral spatial resolution as a function of the axial position. d) The axial spatial resolution measured as a function of the axial position. e) *Enface* image of the USAF resolution target measured at the focal position of 950 nm wavelength.

air at depths of 0.35, 0.9, and 1.3 mm, respectively. The axial spatial resolution of the nanoparticles was found to be similar to values measured in the air. A change in these parameters would depend on several factors such as the refractive index of the sample, dispersion of the sample, surface properties of the sample, and the position of the sample from the lens.

2.2. Biological Sample Imaging

To test the potential of the CCM system to image biological samples, we imaged a swine cornea *ex vivo* acquired from a local butcher shop. The imaging of cornea *ex vivo* did not require any approval from the ethical review board. The volumetric image

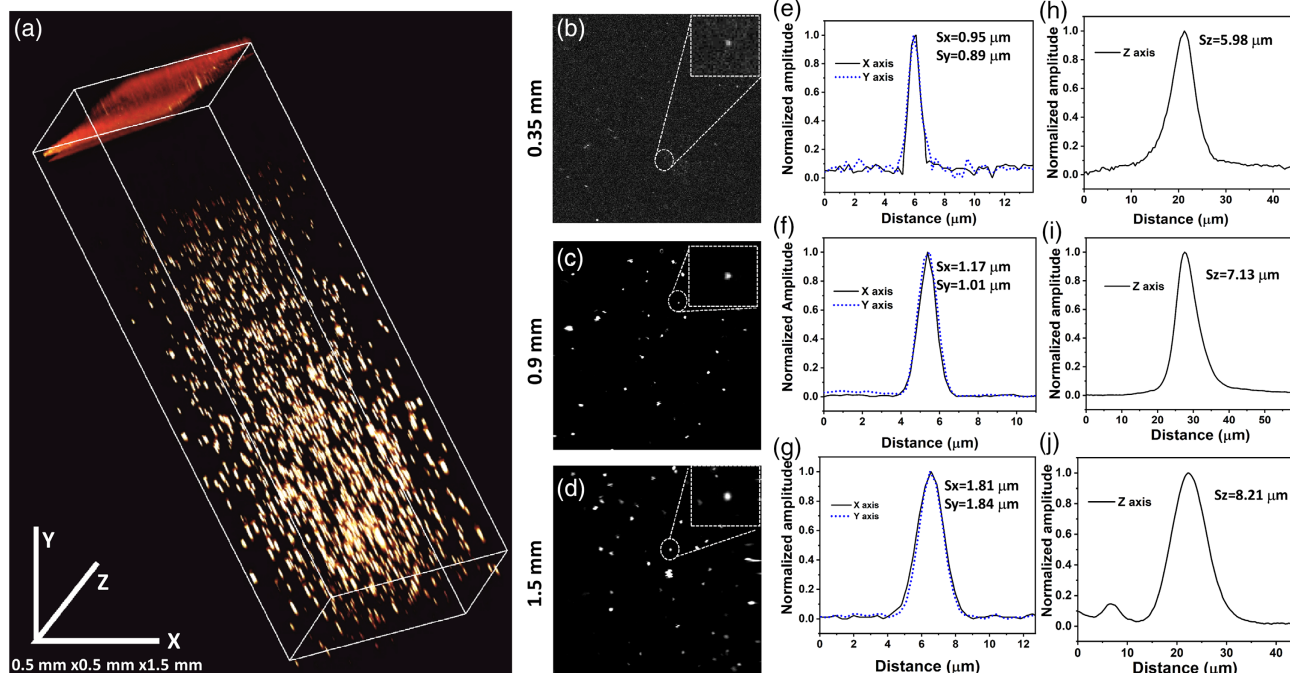


Figure 3. Volumetric imaging of iron oxide nanoparticle phantom. a) 3D image of the iron oxide nanoparticle phantom. Enface images of the nanoparticles at the depth of b) 0.35 mm, c) 0.9 mm, and d) 1.3 mm. X-, Y-axis intensity profile of the smallest nanoparticle at the depth of e) 0.35 mm, f) 0.9 mm, and g) 1.3 mm. Z-axis intensity profile of the smallest nanoparticle at the depth of h) 0.35 mm, i) 0.9 mm, and j) 1.3 mm.

(0.5 mm × 0.5 mm × 1.5 mm), and the enface images of the cornea (0.5 mm × 0.5 mm) at three different locations (at the top, the middle, and the bottom of the cornea) are shown in **Figure 4a–d** respectively. From the enface images of the cornea at different depths, one can see different cellular features. Around the top of the cornea (**Figure 4b**), the epithelial cells are seen. In the middle of the cornea (**Figure 4c**), fibrous structures of the stroma can be seen.

2.3. Surface Profiling

An important application of the CCM system is in the field of surface profiling. For this, we measured the minimum height change that one can measure using our device. To do so, we placed a mirror at the focal position of 700 nm wavelength and monitored the peak position of the reflected signal which is shown in **Figure 5a**. The data was acquired at 51.2 kHz sampling rate. The standard deviation of the peak position was measured to be 14 nm. Further, we introduced a controlled displacement in the mirror placed at the sample position using a piezoelectric stage. The displacement measured by our device when the piezostage was driven with a sinusoidal voltage for ≈50, and ≈900 nm displacement is shown in **Figure 5b,c** respectively.

Furthermore, we performed the surface profiling of an in-house-fabricated microfluidic channel to demonstrate the height profiling feasibility of our device. The microfluidic channel was designed with a channel of varying width but of a constant height of 30 μm. In **Figure 6**, we show the volumetric reconstruction of the microfluidic channel (**Figure 6a**) and a

B-Scan (**Figure 6b**) to show the height profile of one of the narrow channels.

The intensity profile at the location of asterisks within **Figure 6b** as a function of distance is shown in **Figure 6c**. The measured dimensions of the microfluidic channel match very well with the designed dimensions and were verified independently with an OCT system.

3. Discussion and Conclusion

We have developed a long imaging range chromatic confocal system using just a single lens. It can be argued that the technique is too simple but we believe that it is the simplicity of this method that will make it impactful. Conventionally, lenses based on materials such as fused silica and quartz are used in the visible–NIR range due to their excellent optical quality and high transmission of ≈90%. These materials have an Abbe number of around 50. Zinc selenide has an Abbe number ≈8 for visible wavelengths, making it, to the best of our knowledge, the lowest Abbe number material, which is commercially available for the visible/NIR wavelengths. However, ZnSe is rarely used for visible wavelengths because of its low transmission, around 50% for 550 nm and 60% for 600 nm and above. Even though ZnSe has a low transmission in the visible and NIR range, it makes a great candidate for chromatic confocal microscopy because of its high chromatic dispersion. Furthermore, due to the availability of powerful laser sources and sensitive detectors, the low transmission of ZnSe material poses a little challenge. In this work, we have utilized the chromatic dispersion property of a single ZnSe

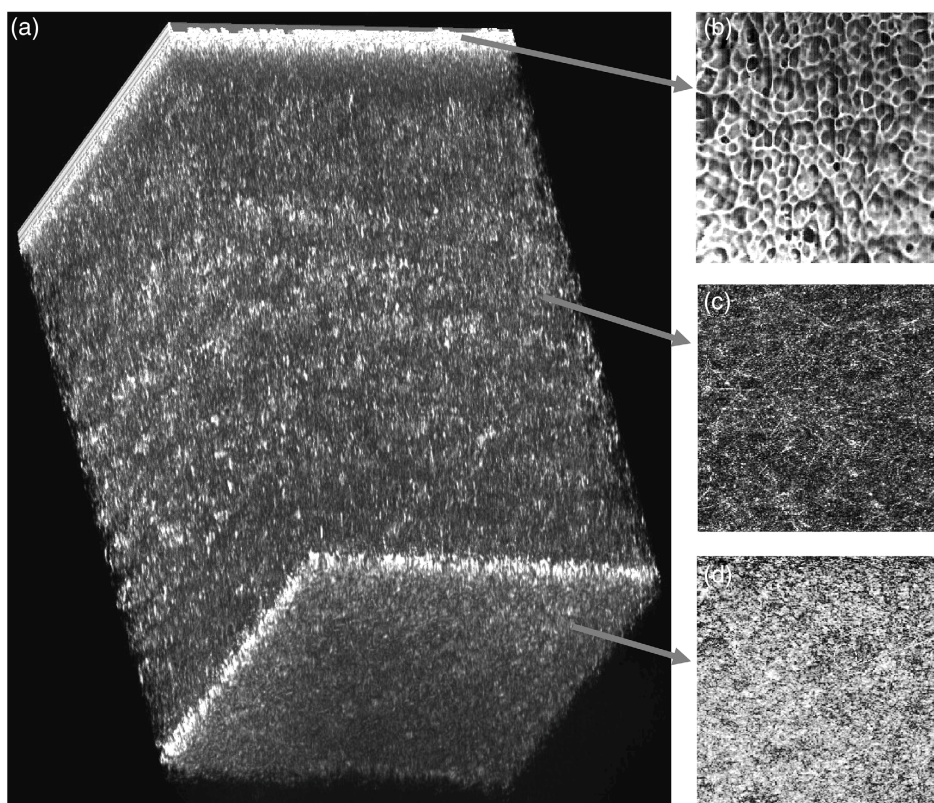


Figure 4. Confocal images of the cornea tissue. a) 3D reconstruction of the cornea ($0.5 \text{ mm} \times 0.5 \text{ mm} \times 1.5 \text{ mm}$). Enface image of the b) top corneal surface ($0.5 \text{ mm} \times 0.5 \text{ mm}$), c) middle of the cornea ($0.5 \text{ mm} \times 0.5 \text{ mm}$), and d) below the cornea ($0.5 \text{ mm} \times 0.5 \text{ mm}$).

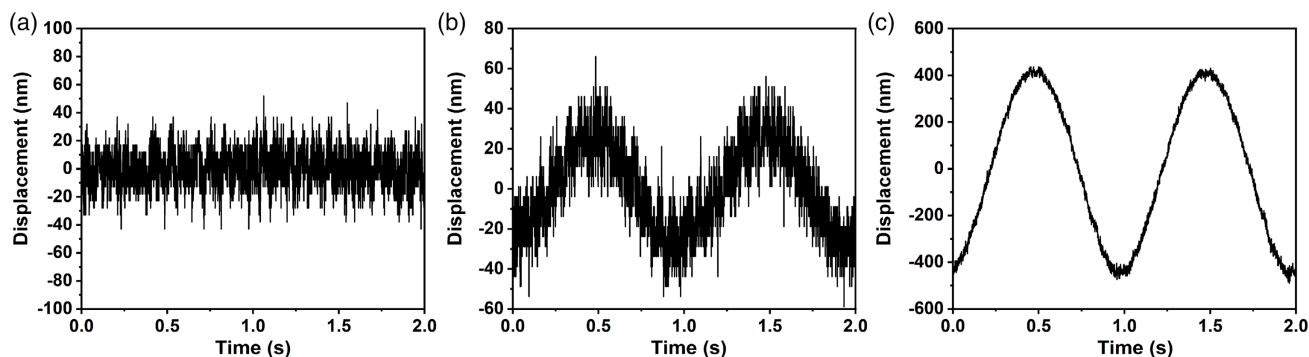


Figure 5. Height profiling accuracy measurement. a) Displacement measured for a static mirror which represents the noise of the system in terms of displacement measurement. The measured displacement of the mirror placed on a piezoelectric stage when driven with a sinusoidal voltage for b) $\approx 50 \text{ nm}$ and c) $\approx 900 \text{ nm}$ displacement.

lens (50.8 mm focal length) to realize a CCM system with an imaging range of 1.8 cm ($\pm 68 \text{ nm}$) with an average lateral spatial resolution of $2.46 \mu\text{m}$ ($\pm 44 \text{ nm}$). Using a 6.37 mm focal length ZnSe lens, we could improve the average lateral spatial resolution to $0.87 \mu\text{m}$ ($\pm 30 \text{ nm}$) with an imaging range of 1.55 mm ($\pm 14 \text{ nm}$).

Besides ZnSe, Gallium phosphide (GaP) is another material that can be used for extended imaging range CCM devices as it also has a low Abbe number of ≈ 6 in the visible range. However, it has not been used for commercial lens fabrication

due to the release of dangerous substances during the fabrication process.^[27] Furthermore, although ZnSe lenses are commercially available, care should be taken while handling these lenses as ZnSe material is also known to be a hazardous material.

In general, the aspheric lenses are corrected for the spherical aberrations but only for a certain wavelength. As we move away from the spherically corrected wavelength, the aberrations increase and reduce the image quality. The ZnSe lens used in our system was designed for $10 \mu\text{m}$ wavelength and therefore

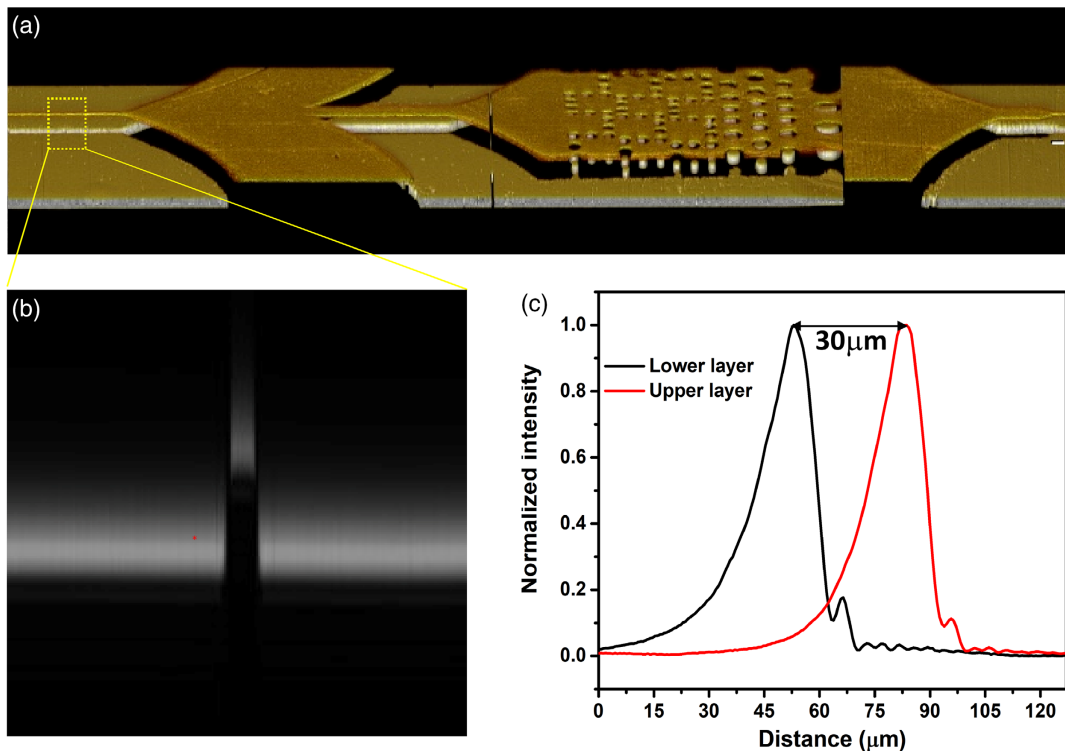


Figure 6. Height profile measurement. a) Volumetric 3D reconstruction of the microfluidic channel chip. b) B-Scan of the microfluidic channel at the position indicated by the box. c) Intensity profile of the two layers as a function of distance at locations indicated by the asterisks (black and red) in (b).

spherically corrected for wavelengths around this wavelength only. If this lens is used for focusing a collimated NIR/IR beam of light, the spherical aberrations would deteriorate the focal spot significantly. Therefore, we used a diverging beam from the output of the optical fiber which allowed us to minimize the spherical aberration for the visible–NIR wavelengths. Depending on the NA of the optical fiber, the distance between the fiber exit and the ZnSe lens can be adjusted to minimize the spherical aberrations for a certain wavelength. We used this methodology to design our system and the distance between the fiber tip and the front surface of the lens was adjusted to minimize the spherical aberrations for 700 nm. The spherical aberrations for the rest of the spectrum were not fully compensated but it still allowed us to achieve an average lateral spatial resolution of $0.87 \mu\text{m}$ ($\pm 30 \text{ nm}$) and $2.46 \mu\text{m}$ ($\pm 44 \text{ nm}$) for 6.35 and 50.8 mm focal length lenses, respectively. The image quality can be further improved using spatially variant point spread function deconvolution algorithms such as Richardson–Lucy Algorithm. The usefulness of such computational deconvolution methods has already been demonstrated for 2D^[28] and 3D^[29,30] imaging applications.

Similar to other point scanning confocal microscopes, our device is also limited in terms of image acquisition speed. The current system allows us to acquire full volumetric data ($512 \times 512 \times 2048$ pixels) in $\approx 5.12 \text{ s}$ which can be improved further using a fast scanner and camera combination.

One important aspect that we should clarify is that although our approach provides an extended imaging range, the penetration depth in the sample is still limited and will be dictated by the

sample properties such as absorption and scattering. For instance, the penetration depth of the visible wavelengths in a biological sample is typically a few hundred micrometers and it can be argued that the extended imaging range that our approach provided is not usable. This would be true if the biological samples were perfectly flat, which is not always the case. For example in a coronary artery with calcified plaque,^[31] the surface height can change by a few millimeters because of the calcification below the surface. Also, the tissue surface of the gastrointestinal tract is highly irregular,^[32] and for imaging of such tissue, not only penetration depth but also an extended imaging range is required.

Cellular-level 3D imaging of biological samples is an obvious application of a confocal microscope but another important application for a chromatic confocal microscope is height profiling. Using a 6.37 mm focal length ZnSe lens, our CCM device would allow one to measure the height profile up to 1.55 mm with a height accuracy of 14 nm and an average lateral spatial resolution of $0.87 \mu\text{m}$. Several such devices are commercially available where chromatic aberrations of standard lenses are used for the axial separation of the spectral components. The reflected light from the sample is acquired in the confocal configuration and the peak of the reflected spectrum is used to measure the height profile of the sample. As an example, one of the commercially available systems (IFS2407-0,1, from Micro-Epsilon), which has a lateral spatial resolution of $3 \mu\text{m}$ (comparable with our system), provides an imaging range of 100 μm . Using a 50.8 mm focal length ZnSe lens, our CCM device could achieve an imaging range of 1.8 cm, which is 180 times greater than the

commercially available device. Our CCM system design not only allowed us to use the commercially available lenses but also the fact that only a single lens is required for 3D imaging makes the system very attractive for both commercial and biological applications.

In conclusion, we have designed and developed a single ZnSe-based chromatic confocal microscopy system with an imaging range of 1.8 cm and with an average lateral spatial resolution of 2.4 μm . For high-resolution biological applications, using a shorter focal length lens, the average lateral spatial resolution can be improved further to 0.87 μm with an imaging range of 1.55 mm. Our device is capable of imaging biological samples in 3D at cellular resolution and can perform surface profiling of biological as well as industrial samples with an unmatched combination of lateral spatial resolution and imaging range. We believe that this advancement will find several applications in biomedical and industrial fields such as imaging of calcified plaque,^[31] gastrointestinal tract,^[32] epithelial tissue,^[16] field-effect transistors,^[3] etc.

4. Experimental Section

For a CCM system, one needs to consider mainly two aspects. First, the NA of the system should be as high as possible to achieve the best possible resolution. Second, the axial focal separation among different wavelength components should be increased significantly to achieve the maximum possible imaging range. However, there is a trade-off between the imaging range and the lateral spatial resolution. The resolution can be improved using a high-NA objective, but this, in turn, reduces the imaging range and vice versa.

We simulated our design using OpticStudio software (Zemax LLC, UK) to optimize the aforementioned parameters. To be able to achieve maximum axial separation between different wavelength components, the chromatic dispersion property of the material was utilized. The chromatic dispersion of a material can be estimated by the Abbe number; the lower the Abbe number, the higher is the chromatic dispersion of the material. ZnSe had an Abbe number of 8 in the visible wavelength range and was the smallest Abbe number material we could find whose lenses were commercially available. It had a transmission of more than 50% for the wavelength range of 0.55–15 μm . Using the OpticStudio software, we simulated the

performance of three commercially available ZnSe lenses having a focal length of 6.35 mm (39 469, Edmund Optics, UK), 12.7 mm (39 471, Edmund Optics, UK), and 50.8 mm (39 495, Edmund Optics, UK) at 10 μm wavelength.

It should be noted that all of these lenses are designed to focus a collimated beam and corrected for the spherical aberration at 10 μm wavelength. However, we used these lenses in the visible and NIR wavelength range. It is feasible because of the reasonable transmission of ZnSe at these wavelengths. However, these lenses cannot be used to focus a collimated visible/NIR beam without introducing significant spherical aberrations and thus degrading the lateral spatial resolution. We circumvented this issue using a diverging beam from the fiber tip (instead of a collimated beam), which was focused using the ZnSe lens. For a diverging beam, with a certain NA, at a certain wavelength, there is a fixed distance of the lens from the fiber tip for which the aspherical aberrations are minimum at the focal position. Using the simulations, we calculated the distance between the lens and the fiber tip for which the 700 nm wavelength had the minimum spherical aberrations. For this fixed distance between the lens and the fiber tip, parameters for the other wavelengths of the spectrum, that is, 500 and 950 nm, were simulated. For all the simulations, the fiber NA of 0.14 was considered.

For developing the CCM device, we utilized a SCL (SC-Pro, YSL Photonics, China). The experimental design is shown in **Figure 7**. The broadband light from the laser was steered through mirrors M1 and M2. The mirror M1 used in the setup was a dichroic mirror (DMPL950T, Thorlabs Inc., USA), which reflected wavelengths up to 950 nm only. The higher wavelengths were transmitted through the mirror M1 and were blocked using a beam block. The light from the mirror M2 was coupled in the input arm 1) of a 75/25 single-mode optical coupler (TW670R3A2, Thorlabs Inc. USA) with a core diameter of 3.5 μm (single-mode cutoff wavelength 570 nm) using lens L1 (M-10X, Newport Corporation, USA). The diverging light at the output arm 2) of the fiber coupler was focused using the ZnSe lens at the sample position. The focused spot size at the sample depends on the mode profile of the laser output from the fiber coupler (which can be multimode at wavelength <570 nm) and the ZnSe lens performance at this wavelength. Ideally one should use a fiber that is single mode at all the wavelengths but unfortunately, broadband fiber couplers based on such fibers are not commercially available yet. The optical power at the sample was measured to be 17 mW, which was lower than the power used in standard laser scanning confocal microscopes.^[33,34] The scattered light from the sample was coupled back to the

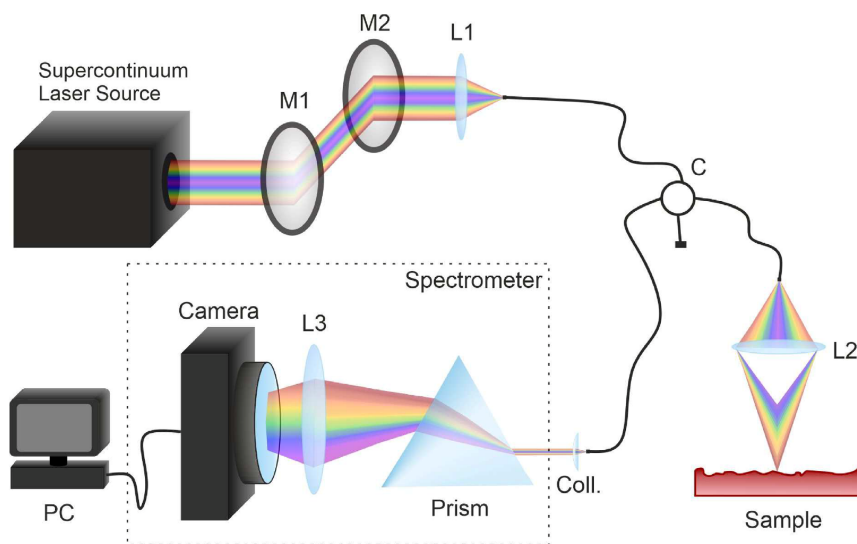


Figure 7. Experimental setup for the realization of the chromatic confocal microscopy device. Mirror (M), Lens (L), Personal computer (PC), Collimator (Coll).

output arm (2) of the coupler and directed to the spectrometer using arm (3). The output arm (4) of the fiber coupler can be used to monitor the laser power and spectrum. For imaging, the beam over the sample was scanned by 0.5 mm at 100 Hz using an amplified piezoelectric actuator (APF710, Thorlabs Inc. USA) along fast imaging axis and by 0.5 mm at a speed of 0.1 mm s^{-1} using a precision translation stage (MBT616D/M Thorlabs Inc., USA) along slow imaging axis. An area of $0.5 \text{ mm} \times 0.5 \text{ mm}$ was scanned using the scanning stages and 512×512 axial scans were acquired to reconstruct the 3D volumetric images of the sample. Each axial scan represented a depth of 1.55 mm and consisted of 2048 pixels. Within the spectrometer, different wavelength components of the light were spatially separated using a prism (PS855, Thorlabs Inc., USA) and focused on a linear charge coupled device camera (ral2048, Basler AG, Germany) sensor working at 51.2 kHz line rate using an objective lens (AF Nikkor 85 mm, Nikon, Japan). The combination of the camera and the scanning module allowed us to acquire the full volumetric data ($512 \times 512 \times 2048$ pixels) in $\approx 5.12 \text{ s}$. We used a prism instead of a grating in the spectrometer because it provides higher transmission efficiency over a broad spectrum. Also, we chose AF Nikkor 85 mm lens in our spectrometer because it has an average transmission of more than 80% in the wavelength range used in this study.

We calibrated the imaging range of our system by placing a mirror at the sample position and moving it axially using a precision translation stage (MBT616D M⁻¹ Thorlabs Inc., USA). To demonstrate the 3D imaging capabilities of our device with high resolution over the imaging range, we performed volumetric imaging of a nanoparticle phantom (OCTPHANTOMS.ORG, UK) with particle size $< 1 \mu\text{m}$. Further, we measured the point spread function of the nanoparticles at different depths. The potential of the device for imaging the biological samples was demonstrated by imaging the microscopic features in an ex vivo swine cornea sample in 3D.

Furthermore, as chromatic confocal microscopes were extensively used in the industry for the height profiling^[13] of the samples, we also tested the feasibility of our device for the same. In this direction, we measured the height measurement accuracy of our device by placing a mirror (at the sample position) on a piezoelectric stage and measured the movement of the piezostage at different driving voltages. The efficacy of the height profiling of the CCM system was demonstrated by measuring the height of microfluidic channels on a chip.

Acknowledgements

G.S. would like to thank Professor Jochen Guck for funding her research. The authors thank Dr. Girardo for providing microfluidic channel for height profiling measurements.

Conflict of Interest

Authors have filed for a patent on the technique developed in this work.

Data Availability Statement

The data that support the findings of this study are available from the corresponding author upon reasonable request.

Keywords

chromatic confocal microscopy, multifocal, surface profiling

Received: April 20, 2022

Revised: September 17, 2022

Published online:

- [1] D. Huang, E. A. Swanson, C. P. Lin, J. S. Schuman, W. G. Stinson, W. Chang, M. R. Hee, T. Flotte, K. Gregory, C. A. Puliafito, *Science* **1991**, 254, 1178.
- [2] M. Minsky, *Rapport technique, Patent* **1955**, 3, 14.
- [3] K. Shi, P. Li, S. Yin, Z. Liu, *Opt. Express* **2004**, 12, 2096.
- [4] B.-C. Chen, W. R. Legant, K. Wang, L. Shao, D. E. Milkie, M. W. Davidson, C. Janetopoulos, X. S. Wu, J. A. Hammer III, Z. Liu, *Science* **2014**, 346, 1257998.
- [5] L. Liu, J. A. Gardecki, S. K. Nadkarni, J. D. Toussaint, Y. Yagi, B. E. Bouma, G. J. Tearney, *Nat. Med.* **2011**, 17, 1010.
- [6] J.-A. Conchello, J. W. Lichtman, *Nat. Methods* **2005**, 2, 920.
- [7] E. Wang, C. M. Babbey, K. W. Dunn, *J. Microsc.* **2005**, 218, 148.
- [8] C.-M. Chia, S. Vyas, T.-H. Wu, J. A. Yeh, Y. Luo, *Appl. Opt.* **2021**, 60, B141.
- [9] A. Badon, S. Bensussen, H. J. Gritton, M. R. Awal, C. V. Gabel, X. Han, J. Mertz, *Optica* **2019**, 6, 389.
- [10] M. Duocastella, G. Vicidomini, A. Diaspro, *Opt. Express* **2014**, 22, 19293.
- [11] R. Shi, C. Jin, H. Xie, Y. Zhang, X. Li, Q. Dai, L. Kong, *Biomed. Opt. Express* **2019**, 10, 6625.
- [12] M. Petrař, M. Hadravsky, M. D. Egger, R. Galambos, *J. Opt. Soc. Am.* **1968**, 58, 661.
- [13] H. J. Tiziani, H. M. Uhde, *Appl. Opt.* **1994**, 33, 1838.
- [14] H. J. Tiziani, R. Achi, R. N. Kramer, *J. Mod. Opt.* **1996**, 43, 155.
- [15] S. Cha, P. C. Lin, L. Zhu, P.-C. Sun, Y. Fainman, *Appl. Opt.* **2000**, 39, 2605.
- [16] C. Olsovsky, R. Shelton, O. Carrasco-Zevallos, B. E. Applegate, K. C. Maitland, *Biomed. Opt. Express* **2013**, 4, 732.
- [17] S. Li, R. Liang, *Appl. Opt.* **2020**, 59, 4349.
- [18] C. Chen, W. Song, J.-W. Chen, J.-H. Wang, Y. H. Chen, B. Xu, M.-K. Chen, H. Li, B. Fang, J. Chen, H. Y. Kuo, S. Wang, D. P. Tsai, S. Zhu, T. Li, *Light Sci. Appl.* **2019**, 8, 99.
- [19] P. C. Lin, P.-C. Sun, L. Zhu, Y. Fainman, *Appl. Opt.* **1998**, 37, 6764.
- [20] S. L. Dobson, P.-C. Sun, Y. Fainman, *Appl. Opt.* **1997**, 36, 4744.
- [21] W. Lyda, M. Gronle, D. Fleischle, F. Mauch, W. Osten, *Meas. Sci. Technol.* **2012**, 23, 054009.
- [22] B. S. Chun, K. Kim, D. Gweon, *Rev. Sci. Instrum.* **2009**, 80, 073706.
- [23] T. Kim, S. H. Kim, D. Do, H. Yoo, D. Gweon, *Opt. Express* **2013**, 21, 6286.
- [24] J. Garzon R, J. Meneses, G. Tribillon, T. Gharbi, A. Plata, *J. Opt. A-Pure Appl. Op.* **2004**, 6, 544-.
- [25] J. Garzon, T. Gharbi, J. Meneses, *J. Opt. A-Pure Appl. Op.* **2008**, 10, 104028.
- [26] J. TrAGARDh, K. Macrae, C. Travis, R. Amor, G. Norris, S. H. Wilson, G. L. Oppo, G. McConnell, *J. Microsc.* **2015**, 259, 66.
- [27] J. Vaclavik, D. Vapenka, *EPJ Web Conf.* **2013**, 48, 00028.
- [28] T. Lauer, in *Deconvolution With A Spatially Variant PSF* Vol. 4847, SPIE, Bellingham, Washington, **2002**, pp. 167–173.
- [29] N. Dey, L. Blanc-Feraud, C. Zimmer, P. Roux, Z. Kam, J. C. Olivo-Marin, J. Zerubia, *Microsc. Res. Tech.* **2006**, 69, 260.
- [30] M. Temerinac-Ott, O. Ronneberger, R. Nitschke, W. Driever, H. Burkhardt, in *Spatially-Variant Lucy-Richardson Deconvolution for Multiview Fusion of Microscopical 3D Images*, IEEE, Piscataway, NJ, **2011**, pp. 899–904.
- [31] H. Mori, S. Torii, M. Kutyna, A. Sakamoto, A. V. Finn, R. Virmani, *JACC Cardiovasc. Imag.* **2018**, 11, 127.
- [32] M. J. Gora, J. S. Sauk, R. W. Carruth, K. A. Gallagher, M. J. Suter, N. S. Nishioka, L. E. Kava, M. Rosenberg, B. E. Bouma, G. J. Tearney, *Nat. Med.* **2013**, 19, 238.
- [33] A. Gerger, S. Koller, T. Kern, C. Massone, K. Steiger, E. Richtig, H. Kerl, J. Smolle, *J. Invest. Dermatol.* **2005**, 124, 493.
- [34] R. Alvarez-Roman, A. Naik, Y. N. Kalia, H. Fessi, R. H. Guy, *Eur. J. Pharm. Biopharm.* **2004**, 58, 301.